

# Rethinking Vision Transformer for Object Centric Foundation Models

Manuel Traub<sup>1</sup> Martin V. Butz<sup>1</sup>

## Abstract

Recent state-of-the-art object segmentation mechanisms, such as the Segment Anything Model (SAM) and FastSAM, first encode the full image over several layers and then focus on generating the mask for one particular object or area. We present an off-grid Fovea-Like Input Patching (FLIP) approach, which selects image input and encodes it from the beginning in an object-focused manner. While doing so, it separates locational encoding from an object-centric perceptual code. FLIP is more data-efficient and yields improved segmentation performance when masking relatively small objects in high-resolution visual scenes. On standard benchmarks such as Hypersim, KITTI-360, and OpenImages, FLIP achieves Intersection over Union (IoU) scores that approach the performance of SAM with much less compute effort. It surpasses FastSAM in all IoU measurements. We also introduce an additional semi-natural but highly intuitive dataset where FLIP outperforms SAM and FastSAM overall and particularly on relatively small objects. Seeing that FLIP is an end-to-end object-centric segmentation approach, it has high potential particularly for applications that benefit from computationally efficient, spatially highly selective object tracking.

## 1. Introduction

Object-centric models have emerged as a powerful paradigm for structured perception in visual tasks. They offer the potential to represent complex scenes in a more interpretable and compositional manner. While traditional architectures such as Convolutional Neural Networks (CNNs) (Liu et al., 2022) and Vision Transformers (ViTs) (Dosovitskiy et al., 2020) have demonstrated impressive performance on large-scale datasets, they often lack the nuanced object-level understanding required for robust scene parsing. Furthermore,

<sup>1</sup>Cognitive Modeling, Department of Computer Science and Department of Psychology, University of Tübingen Sand 14, 72076 Tübingen, Germany. Correspondence to: Manuel Traub <manuel.traub@uni-tuebingen.de>.

these models typically require massive amounts of labeled data and exhibit vulnerabilities to adversarial perturbations.

Recent advances in object-centric learning, such as Slot Attention (Locatello et al., 2020), have sought to address these challenges by enabling the model to discover and represent objects within a scene as distinct entities. Models like SAVi++ (Elsayed et al., 2022), VideoSAUR (Zadaianchuk et al., 2024), and Loci (Traub et al., 2023; 2024a;b) have advanced the state-of-the-art in unsupervised object-centric learning. They are able to disentangle objects from complex backgrounds and track their identities over time. Still, these approaches struggle to scale effectively to more complex, real-world data.

In contrast, the Segment Anything (SAM) model (Kirillov et al., 2023) has introduced a paradigm shift in object-centric learning. SAM learns from a vast array of diverse data that is segmented by a two stage segmentation process. First, a powerful transformer-based foundational model encodes the complete image. Second, a query-based focusing mech-

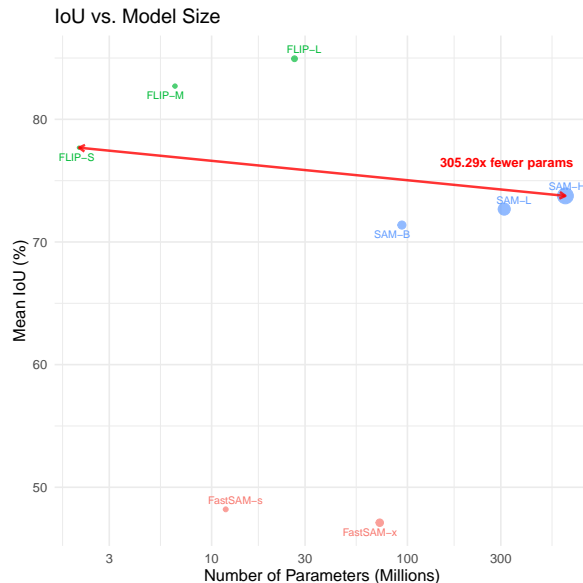


Figure 1. Comparison of segmentation performance (Mean IoU) on our ObjaScale dataset versus model size (number of parameters, in millions). FLIP variants achieve superior performance with significantly fewer parameters compared to SAM variants.

anism specifies which object to segment. Only this second mechanism targets one image area or object and leads to the production of the targeted output mask. SAM marks the state-of-the-art in object segmentation tasks. However, despite its impressive performance, SAM has its limits. First, the transformer-based encoder requires very large computational resources. Second, the encoder backbone encodes the complete image, potentially wasting processing resources, particularly when small objects are to be segmented.

The FastSAM model (Zhao et al., 2023) addresses the former limit. FastSAM replaces the first stage transformer-based encoder architecture in SAM with a convolutional ANN approach (CNN), which is pre-trained to segment the whole image. The query then targets the latent encodings and produces one area- or object-specific mask selectively. As a result, FastSAM yields performance close-to SAM, but is trained on only 2% of the original SAM dataset, has much fewer parameters, and partially runs an order of magnitude faster.

The latter limit remains an open challenge. At this point nearly all segmentation techniques, including SAM and FastSAM, rely on a full image encoder. This is also the case for most object centric models, such as SlotAttention, VideoSAUR, and related work (Locatello et al., 2020; Elsayed et al., 2022; Singh et al., 2022; Zadaianchuk et al., 2024), which first encode the entire image before assigning information to slots. The challenge to computationally efficiently segment and track small but potentially high-resolution objects across diverse and complex scenes remains.

To this end, we introduce FLIP: a fovea-like input patching approach that is integrated in an object-centric, off-grid vision framework. FLIP dynamically adapts its processing pipeline to the object’s size and spatial characteristics. It ignores currently irrelevant image subregions and focusses on critical regions with a flexible, multi-resolution approach. Our key contributions are:

- **Off-Grid, Scale-Invariant Object Encoding:** We introduce a fovea-inspired patch sampling method that directly encodes image regions off-grid, adaptively focusing on objects of interest in a multi-resolution fashion. This scale-invariant approach is robust to large variations in object size and image resolution. It enables the detailed encoding of very small objects even in high-resolution scenes.
- **Interpretable Object-Centric Latent Representation:** Building on insights from cognitive science, FLIP explicitly segregates perceptual features from positional cues into distinct latent embeddings. This structured representation not only boosts segmentation accuracy but also improves explainability, as it allows

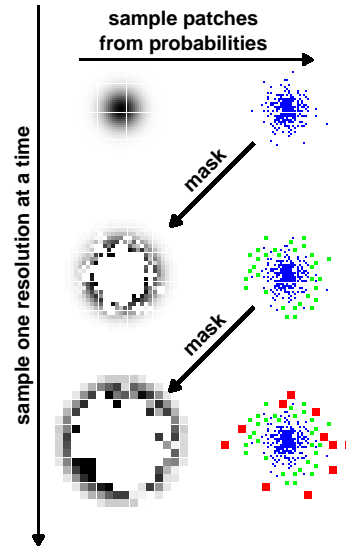


Figure 2. The multi-resolution patch sampling procedure in FLIP sequentially samples tiny (blue), small (green), and large (red) patches given an object-centered 2D Gaussian. Overlapping patches are prohibited, thus generating a fovea-like distribution of patches across multiple resolutions.

for a separated assessment of object identity and spatial placement.

- **State-of-the-Art Segmentation Performance with High Parameter Efficiency:** Despite using significantly fewer parameters compared to state-of-the-art models like SAM or FastSAM, FLIP achieves competitive (SAM) or superior (FastSAM) segmentation accuracy on benchmarks such as Hypersim, KITTI-360, and OpenImages.
- **Superior performance on novel dataset *ObjScale*** For further evaluation, we present a segmentation dataset that contains high-resolution real-world backgrounds combined with objects of varying scales, rendered in Blender. FLIP outperforms all other methods on *ObjScale*, even with the smallest parameter settings (Figure 1). Note that *ObjScale* is used for evaluation only, neither FLIP nor SAM or FastSAM were trained on it.

## 2. Related Work

Several lines of research contain methods that share thematically similar ideas in handling multi-scale objects, dynamic sampling, or biologically inspired foveation. *Deformable Convolutional Networks* (Dai et al., 2017) and their successors (Zhu et al., 2019; Xiong et al., 2024) introduce learnable

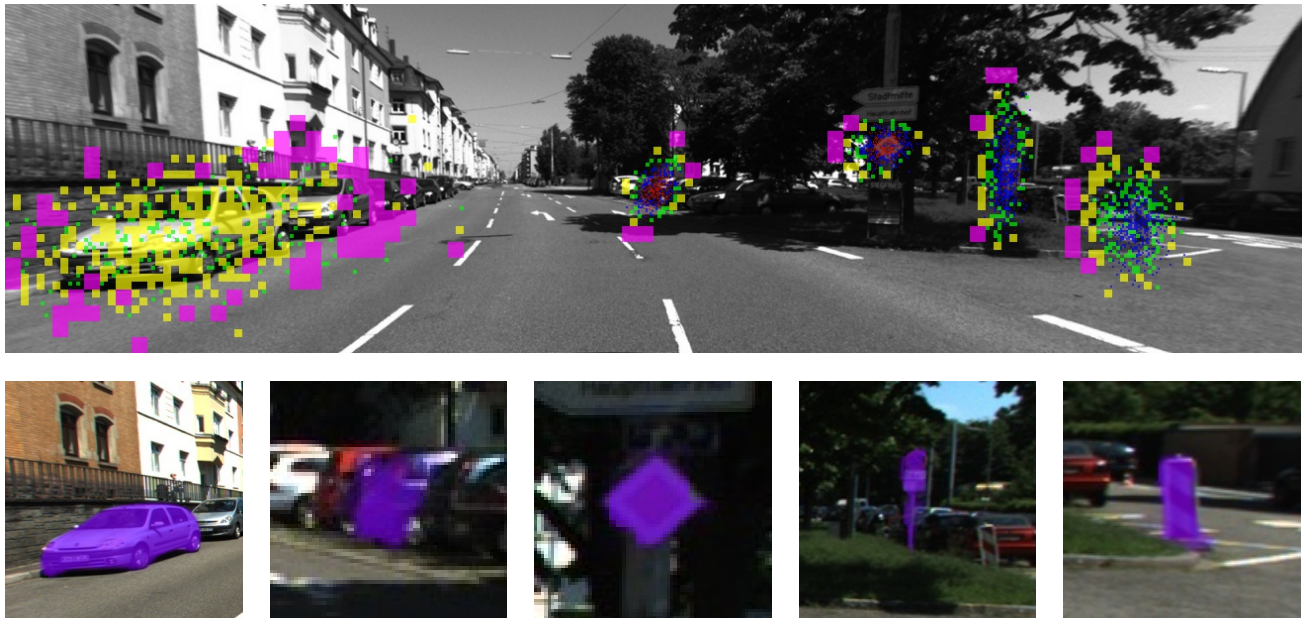


Figure 3. Visualization of our FLIP (Fovea-Like Input Patching) approach applied to an image from the KITTI-360 dataset, showcasing potential applications in autonomous driving. The figure illustrates how our model dynamically focuses on multiple objects within a complex urban scene by allocating multi-resolution patches centered around estimated object locations. Higher-resolution patches (smaller sizes) are concentrated on critical areas such as vehicles and road-signs, emulating a foveal vision system, while lower-resolution patches (larger sizes) cover peripheral regions to enable the consideration of the surrounding context. Patches are color-coded by size: purple for  $16 \times 16$  patches, yellow for  $8 \times 8$ , green for  $4 \times 4$ , blue for  $2 \times 2$ , and red for  $1 \times 1$ .

offsets or selective kernels to better handle varying spatial structures. *Focal Sparse Convolutional Networks* (Chen et al., 2022) focus computation on salient 3D regions in point clouds. Additionally, biologically inspired foveation has been explored in works like (Lukanov et al., 2021; Kapanian et al., 2019; Thavamani et al., 2021).

### 3. Methods

In this section, we present the overall Fovea-Like Input Patching (FLIP) architecture. Its main processing pipeline is shown in Figure 4. FLIP is a supervised vision model for efficient object-centric segmentation. It combines a fovea-inspired patching mechanism with a Vision Transformer (ViT)-based encoder. The encoded information is then used to generate the targeted object’s segmentation mask, location, and bounding box, thereby disentangling perceptual and positional information.

The fovea-like patching mechanism dynamically selects multi-resolution patches based on a 2D Gaussian distribution, which has an effect similar to the query in SAM and FastSAM but acts directly on the input image. High-resolution patches focus on the object center, capturing fine details, while coarser patches cover peripheral regions, which inform FLIP about the surrounding context.

The ViT encoder processes the sampled patches and outputs

two representations: a perceptual code ( $z_p$ ), which captures the object’s appearance and shape, and a positional code ( $z_{pos}$ ), which encodes location, orientation, and scale.

The predictor combines  $z_p$  and  $z_{pos}$  to predict the segmentation mask. The positional code guides dynamic resolution-dependent decoding, ensuring high-resolution predictions at the object’s spatial extent, while the perceptual code provides detailed object-specific information. This design enables FLIP to excel at segmenting small objects in high-resolution scenes with much lower computational overhead when compared to SAM and FastSAM.

FLIP is trained end-to-end with supervised losses for mask prediction, bounding box localization, and positional accuracy. In the following subsections, we provide the mathematical details of the fovea-like sampling mechanism, the ViT encoder, and the ViT predictor.

#### 3.1. Fovea-like Input Patching

We equip our ViT-based model with a multi-resolution, fovea-inspired patching mechanism that centers around the object of interest, thereby preserving high-resolution detail at the object center and coarser coverage in peripheral regions. Specifically, we derive the object center  $\mu = (\mu_x, \mu_y)$  and covariance  $\Sigma$  from the ground-truth mask, yielding a 2D Gaussian  $\mathcal{N}(\mu, \Sigma)$  that approximates the object’s spa-

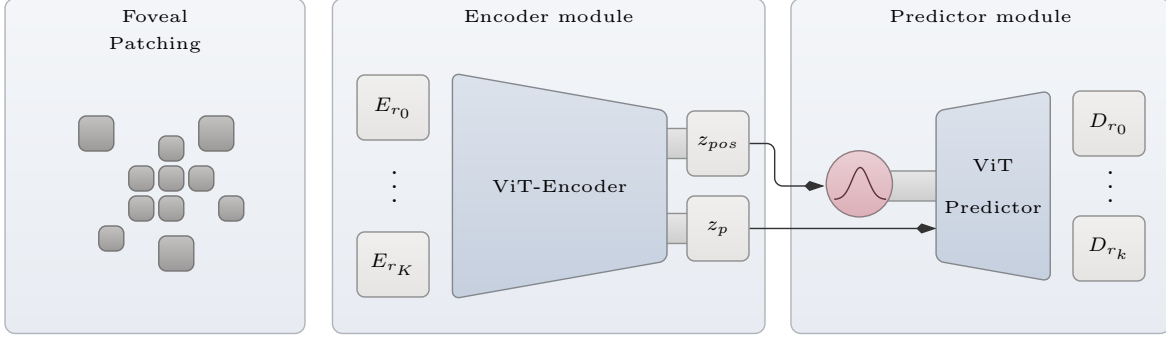


Figure 4. Overview of the FLIP architecture. The Foveal Patching module dynamically samples multi-resolution patches centered around objects of interest. These patches are embedded into a unified latent space using resolution-specific Patch Embedding Modules ( $E_{r_0}$  to  $E_{r_K}$ ). The Vision Transformer Encoder processes the embedded patches, generating separate Perceptual ( $z_p$ ) and Positional Codes ( $z_{pos}$ ). The ViT predictor combines these codes to predict the object instance segmentation mask, reconstructing it via Patch De-embedding Modules ( $D_{r_0}$  to  $D_{r_K}$ ).

tial extent and orientation in compressed form. From  $\Sigma$ , we extract rotation  $(\theta_a, \theta_b)$  and scale  $(\sigma_x, \sigma_y)$  via a standard eigenvalue decomposition of the covariance matrix. For input sampling, the Gaussian serves as a spatial input query—similar to the prompts in SAM and FastSAM—from which we then draw patches at multiple scales.

We define  $K$  patch sizes  $p_1 < p_2 < \dots < p_K$ , from smallest (highest resolution) to largest. We fix the total number of patches  $N$  and choose  $N_i$  patches for patch size  $p_i$  as follows. First, we compute default numbers  $\hat{N}_i$  by approximating the area covered by the Gaussian’s 99% inner density mass from  $\Sigma$  and dividing it by  $p_i^2$ . Then, starting at the coarsest resolution (i.e.,  $p_K$ ), we compute  $N_i = \min(\hat{N}_i, N - \sum_{j=i+1}^K N_j)$ . As a result, all chosen patch sizes are smaller than the Gaussian inner area and the number of chosen patches per size distributes itself from coarse to fine until the total number of patches  $N$  is reached ( $N = \sum_i^K N_i$ ).

We sample  $N_i$  patches from  $\mathcal{N}(\mu, \Sigma)$ . Higher-resolution patches (small  $p_i$ ) are drawn first. Next, progressively larger patches (lower resolution) are sampled from the remaining density excluding the patches that overlap with patches that were already chosen (cf. Figure 2). Each sampled patch is first flattened and then mapped to a common embedding space via resolution-specific encoders  $E_{r_i}$  (similarly to Jaegle et al., 2021), yielding a set of tokens  $T = \{t_1, \dots, t_N\}$  of equal tensor size. These embedded tokens are concatenated and fed to the main ViT layers. Note that because sampling depends on  $\mu$  and  $\Sigma$  only, the approach is in principle independent of the full image size.

### 3.2. Object-Centric Attention

For further encoding, we use modified Transformer blocks that preserve the “what vs. where” separation. Figure 5

shows the design of one block. Inspired by (Yu et al., 2023), we inject positional embeddings in every layer, but only into the queries and keys (never the values), ensuring spatial cues influence attention without affecting perceptual content. The first layer  $l = 1$  block receives as input the set of tokens  $T$ , that is,  $X_1 = T$ . Further, all blocks receive the following positional encoding  $PE$ , in the form of *relative positional embeddings*. We compute these embeddings relative to the 2D Gaussian input query, shifting each token coordinate  $(x_i, y_i)$  by  $(\mu_x, \mu_y)$ , rotating it by  $(\theta_a, \theta_b)$ , and scaling it by  $(\sigma_x, \sigma_y)$ . We then generate the embedding  $PE$  via an MLP. This embedding is then added to queries and keys:

$$PE_i = MLP_i(\hat{x}_i, \hat{y}_i), \quad PE_j = MLP_j(\hat{x}_j, \hat{y}_j), \\ \mathbf{Q}'_i = \mathbf{Q}_i + PE_i, \quad \mathbf{K}'_j = \mathbf{K}_j + PE_j.$$

We adopt a pre-layer normalization scheme (Xiong et al., 2020), such that LayerNorm precedes both the self-attention and FFN blocks. Consequently, the Transformer layer computations for input  $X_l$  proceed as:

$$\hat{X} = \text{LN}(X_l), \\ Q = \hat{X}W_Q, \quad K = \hat{X}W_K, \quad V = \hat{X}W_V, \\ Q' = Q + PE, \quad K' = K + PE, \\ Y = X_l + \text{softmax}\left(\frac{Q'K'^T}{\sqrt{d_k}}\right)V, \\ X_{l+1} = Y + \text{FFN}(\text{LN}(Y)),$$

where  $d_k$  is the key dimension. By avoiding positional biases in  $V$ , the model attends spatially via  $PE$  without affecting the perceptual content. This design aligns with our object-centric principle: positional information modulates attention weights (queries, keys), and perceptual information flows through  $V$ . Depending on the chosen network sizes, we use three, six, or seven of these encoding blocks.



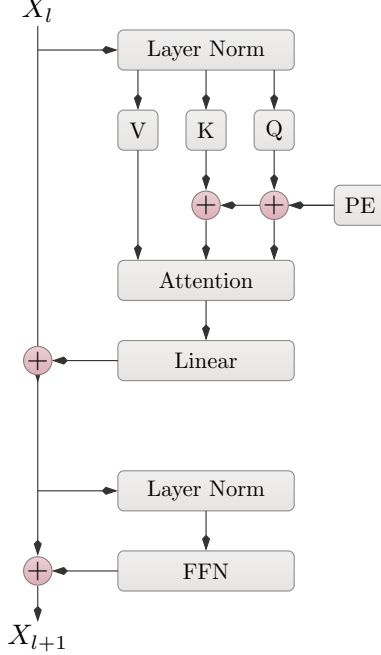


Figure 5. Architecture of the Object-Centric Attention block in FLIP. Positional embeddings influence only the queries and keys, maintaining separation of spatial and perceptual information for efficient object-centric processing.

### 3.3. Learning What and Where

Following the Loci family of models (Traub et al., 2023; 2024a;b), which draw inspiration from the dorsal-ventral visual pathway separation in the brain, FLIP finally enforces a strict separation between perceptual and positional information at the end of the encoding pipeline. This separation ensures that the model independently processes “what” an object is and “where” it is located, encouraging a more interpretable object segmentation. The input to this separation comes from the output of the last object-centric attention block, which can be interpreted as consisting of  $N$  encoded tokens  $t_i$  and associated image coordinates  $(x_i, y_i)$ .

**Perception Code  $\mathbf{z}_p$ .** To generate the final perception code  $\mathbf{z}_p$ , we combine all tokens by average pooling them and refining them via a cross-attention-layer, using the average pooled value as the query:

$$\mathbf{z}_{avg} = \frac{1}{N} \sum_{i=1}^N \mathbf{t}_i$$

$$\mathbf{z}_p = \mathbf{z}_{avg} + \text{CrossAttentionLayer}(\mathbf{z}_{avg}, T).$$

This yields a compact representation of the object’s appearance.

**Positional Code  $\mathbf{z}_{pos}$ .** To infer  $\mathbf{z}_{pos}$ , cross-attention modules on token coordinates obtain object-focused mean position, scale, and orientation estimates. First, we compute the object center:

$$\mathbf{q}_\mu = W_q^\mu \mathbf{1}, \quad \mathbf{k}_{\mu,i} = W_k^\mu t_i, \quad a_{\mu,i} = \text{softmax}(\mathbf{q}_\mu \cdot \mathbf{k}_{\mu,i}^\top),$$

$$\mu_x = \sum_{i=1}^N a_{\mu,i} x_i, \quad \mu_y = \sum_{i=1}^N a_{\mu,i} y_i.$$

Similarly, additional cross-attention heads estimate  $\sigma_x, \sigma_y$  (spread) and  $\theta_a, \theta_b$  (rotation). Concatenating these yields:

$$\mathbf{z}_{pos} = [\mu_x, \mu_y, \sigma_x, \sigma_y, \theta_a, \theta_b],$$

which enables us in principle to use this positional output also as an input query. This option is however not further explored in this paper.

### 3.4. Mask Prediction

To generate mask predictions, we first choose the region of the image that is expected to contain the object. FLIP then generates output patches that cover this region, predicting the mask via the patches. To determine the output region we take the positional code  $\mathbf{z}_{pos}$  and compute the rotated coordinates via:

$$x_{rot} = \theta_a (x - \mu_x) - \theta_b (y - \mu_y)$$

$$y_{rot} = \theta_b (x - \mu_x) + \theta_a (y - \mu_y),$$

with  $\sqrt{\theta_a^2 + \theta_b^2} = 1$  and  $\sigma_x, \sigma_y$  clipped to  $\geq \epsilon$ . The Gaussian map is

$$G(x, y) = \exp\left(-\frac{1}{2} \left[ \left( \frac{x_{rot}}{\sigma_x} \right)^2 + \left( \frac{y_{rot}}{\sigma_y} \right)^2 \right] \right),$$

thresholded at 0.01 (its 99% confidence region).

We fully cover this region, by selecting  $N_{out}$  patches using **two resolutions**. The patch ratio for these resolutions is chosen adaptively from  $\sigma_x, \sigma_y$  to guarantee that exactly  $N_{out}$  patches are needed to cover the determined output region. For each patch  $(x_i, y_i)$  we form an output token:

$$t_{out,i} = \mathbf{z}_p + \text{PE}(x_i, y_i),$$

where  $\mathbf{z}_p$  is the perception code. These tokens are then processed through two Transformer blocks, whose block structure is identical to the encoder blocks. Finally, a resolution-specific de-embedding module  $D_{r_i}$  reconstructs each patch  $\hat{P}_i$ :

$$\hat{P}_i = D_{r_i}(t_{out,i}).$$

By placing each patch  $\hat{P}_i$  at its respective position  $(x_i, y_i)$  we cover the output region with patch-respective mask predictions and set the remaining area to zero (i.e., not part of the mask). This concludes the mask prediction process.



Figure 6. Examples of multi-resolution patch inputs (top row) and corresponding mask predictions (bottom row) from FLIP. Input patches are color-coded by size: purple ( $16 \times 16$ ), yellow ( $8 \times 8$ ), green ( $4 \times 4$ ), blue ( $2 \times 2$ ), and red ( $1 \times 1$ ). Higher-resolution patches focus on object centers for detail, while lower-resolution patches cover peripheral regions for efficiency. Mask predictions show accurate segmentation with optimized resource allocation.

### 3.5. Training

We train FLIP *only* on the Segment Anything Dataset, performing approximately 1.5 M updates at a batch size of 256, covering about 35.84 % of the dataset. Each training example has an associated object mask, from which we compute a 2D Gaussian distribution capturing the object’s center, scale, and orientation. To improve generalization, we apply random perturbations to this Gaussian by slightly shifting  $x$  and  $y$ , stretching or compressing  $\sigma_x$  and  $\sigma_y$ , and introducing small rotations. Tokens are sampled directly from this perturbed 2D Gaussian, with the total number of tokens,  $N$ , varied around a predefined mean  $\mu$  during training to further improve generalization.

The training consists of three phases:

- **Phase 1:** Training begins with a mean token count  $\mu = 128$  and half-resolution inputs for 800k steps.
- **Phase 2:** The token count increases to  $\mu = 512$  with full-resolution inputs for the next 600k steps.
- **Phase 3:** A final fine-tuning phase uses  $\mu = 4096$  tokens for 100k steps, matching the number of patches used by SAM.

We train three model sizes FLIP-S (2.6M parameters), FLIP-M (6.5M parameters), and FLIP-L (26.5M parameters). Notably, these models are significantly smaller in parameter count than SAM variants (up to 641.1M) and FastSAM-x (72.2M), with only FastSAM-s falling in a similar range (11.8M).

We optimize three losses to predict accurate masks, bounding boxes, and positional ( $\mathbf{z}_{\text{pos}}$ ) codes.

- **Mask Loss:** Binary cross-entropy loss between predicted mask logits  $\hat{M}$  and ground truth  $M$ :

$$s_{\text{mask},i} = \frac{1}{\sum_{j=1}^{N_i} M_{ij}}$$

$$\mathcal{L}_{\text{mask}} = \frac{1}{B} \sum_{i=1}^B s_{\text{mask},i} \sum_{j=1}^{N_i} \ell_{\text{BCE}}(\hat{M}_{ij}, M_{ij}),$$

where  $B$  is the batch size.

- **Position Loss:** Penalizes deviations in mean position ( $\mu$ ), scale ( $\sigma$ ), and rotation ( $\theta$ ):

$$\mathcal{L}_{\text{pos}} = \frac{1}{B} \sum_{i=1}^B \left( \frac{1}{\sigma_i} \|\hat{\mu}_i - \mu_i\|^2 + \|\hat{\sigma}_i - \sigma_i\|^2 + \|\hat{\theta}_i - \theta_i\|^2 \right).$$

- **Bounding Box Loss:** Matches predicted bounding boxes  $\hat{B}_i$  to ground truth  $B_i$ :

$$\mathcal{L}_{\text{bbox}} = \frac{1}{B} \sum_{i=1}^B \frac{1}{\sigma_i} \|\hat{B}_i - B_i\|^2.$$

**Total Loss** The overall loss combines mask, position, and bounding box losses:

$$\mathcal{L}_{\text{stage1}} = \mathcal{L}_{\text{mask}} + \lambda_{\text{pos}} \mathcal{L}_{\text{pos}} + \lambda_{\text{bbox}} \mathcal{L}_{\text{bbox}},$$

where  $\lambda_{\text{pos}}$  and  $\lambda_{\text{bbox}}$  control weightings.

## 4. Results

We evaluate FLIP on our newly constructed synthetic dataset ObjScale, which we designed to stress-test scale invariance,

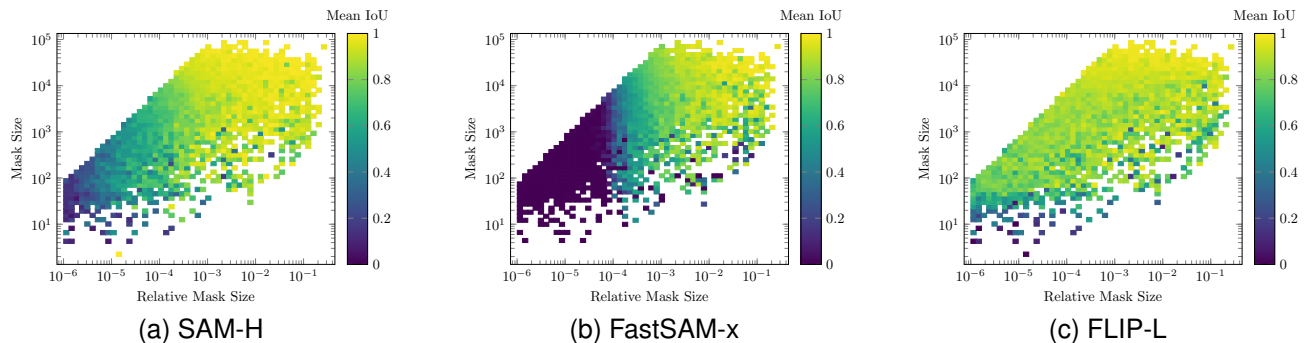


Figure 7. IoU (ObjaScale) heatmaps illustrating relative vs. absolute mask size. FLIP-L retains strong accuracy even for small objects, provided there are enough pixels (e.g.,  $\geq 10 \times 10$ ).

Table 1. Comparison of Mean IoU (%) and Std IoU (%) across different datasets.

Model	Size (M)	Time (ms)			Hypersim	KITTI-360	OpenImage	ObjaScale (ours)
		Pre/Pos	Model	Total	Mean $\pm$ Std IoU (%)	Mean $\pm$ Std IoU (%)	Mean $\pm$ Std IoU (%)	Mean $\pm$ Std IoU (%)
FastSAM-s	11.8	4.56	4.84	9.40	36.80 $\pm$ 34.62	37.71 $\pm$ 32.76	61.14 $\pm$ 32.10	48.20 $\pm$ 35.69
FastSAM-x	72.2	4.54	18.46	23.00	43.39 $\pm$ 35.95	38.92 $\pm$ 34.06	69.31 $\pm$ 29.25	47.11 $\pm$ 36.41
FLIP-S (ours)	2.1	22.58	9.63	32.21	61.51 $\pm$ 27.16	59.30 $\pm$ 19.58	70.75 $\pm$ 23.51	77.69 $\pm$ 19.83
FLIP-M (ours)	6.5	23.84	15.04	38.88	64.36 $\pm$ 28.32	61.45 $\pm$ 19.64	76.76 $\pm$ 21.73	82.71 $\pm$ 18.24
FLIP-L (ours)	26.5	22.54	18.09	40.63	66.83 $\pm$ 27.74	61.85 $\pm$ 19.56	78.37 $\pm$ 21.77	84.94 $\pm$ 17.16
SAM-B	93.7	11.06	63.40	74.46	71.46 $\pm$ 20.88	62.38 $\pm$ 21.41	84.72 $\pm$ 15.38	71.38 $\pm$ 25.36
SAM-L	312.3	11.07	139.17	150.24	72.13 $\pm$ 21.21	62.73 $\pm$ 20.31	86.94 $\pm$ 13.41	72.68 $\pm$ 25.22
SAM-H	641.1	10.96	222.00	232.96	72.37 $\pm$ 21.65	62.47 $\pm$ 20.52	87.06 $\pm$ 13.53	73.76 $\pm$ 24.59

and on three standard benchmarks: Hypersim, KITTI-360, and OpenImages (Roberts et al., 2021; Liao et al., 2022; Kuznetsova et al., 2020). Notably, FLIP was neither trained nor fine-tuned on the ObjScale dataset. Our experiments compare FLIP against two state-of-the-art segmentation methods, SAM (Kirillov et al., 2023) and FastSAM (Zhao et al., 2023), focusing on handling small objects, achieving high IoU, and balancing parameter/runtime trade-offs.

#### 4.1. Experimental Setup and Dataset Creation

We selected 68 diverse categories from Objaverse (Deitke et al., 2023) and combined each with high-resolution HDRI Haven (Zaal, Greg) backgrounds in Blender, yielding 10,200 synthetic images, which form our ObjScale dataset. Object scale and image resolution (ranging from 512 to 8192) were randomized, producing masks spanning minuscule ( $< 0.0001\%$ ) to large fractions of the image (Fig. 8). For SAM and FastSAM, bounding-box prompts computed from ground-truth masks were used; FLIP employed 2D Gaussian prompts by design.

#### 4.2. Performance vs. Relative Mask Size

On the ObjScale dataset, Figure 10 plots IoU against relative mask size. FLIP-L consistently surpasses the other models for small objects ( $< 0.1\%$  of the image). FastSAM-

x drops steeply, while SAM-H tapers more moderately. By adaptively sampling around the actual pixel area, FLIP-L retains strong IoU scores even when objects occupy a tiny fraction of the scene.

#### 4.3. Heatmap Analysis and Small-Object Segmentation

Figure 7 highlights segmentation performance with respect to both relative and absolute mask size on ObjScale. SAM-H struggles when the mask ratio diminishes, and FastSAM-x fails below a mask to image ratio of 0.01%. FLIP-L, by contrast, primarily depends on whether the object covers enough pixels to support a sufficiently detailed patch representation.

#### 4.4. Evaluation on Benchmark Datasets

Table 1 compares Mean and Std IoU across Hypersim, KITTI-360, OpenImages and ObjScale. FLIP exceeds the best FastSAM variant and remains close to SAM, while requiring substantially fewer parameters and competitive inference time. Notably, this is despite its input patch sampling and output patch selection (pre-/pos-processing times) are not yet optimized for inference time.

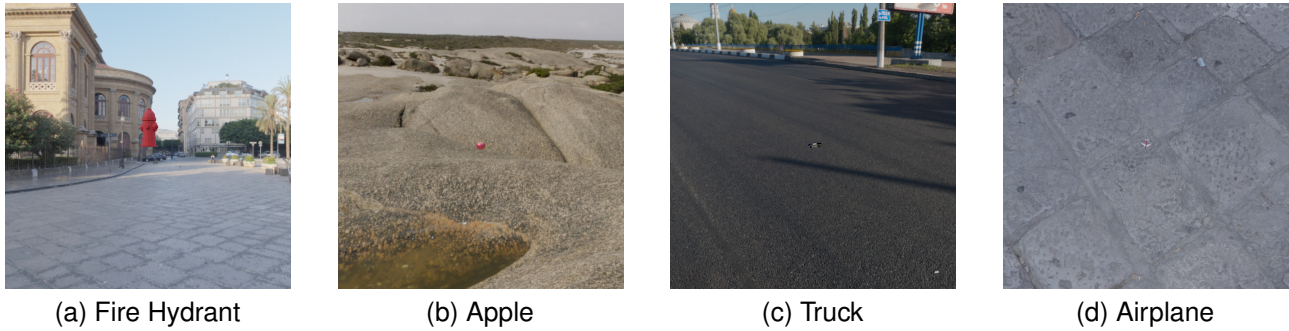


Figure 8. Examples from our synthetic dataset. Objects from various categories—(a) Fire Hydrant, (b) Apple, (c) Truck, and (d) Airplane—are rendered with high-resolution HDRI Haven backgrounds. The dataset includes diverse objects and scene compositions, with varying object scales, resolutions, and viewing angles to challenge segmentation models. Best viewed zoomed in.

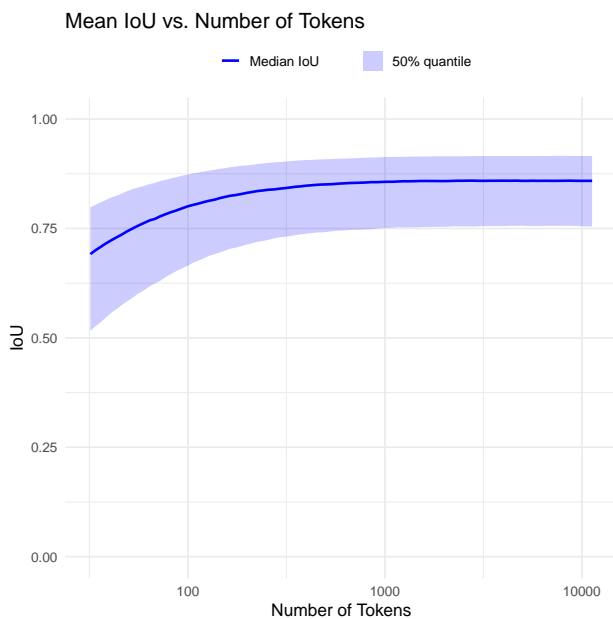


Figure 9. FLIP-L performance on OpenImages under different numbers of sampled patches.

#### 4.5. Varying the Patch Token Budget

Lastly, we evaluated how limiting FLIP’s patch sampling impacts performance. Figure 9 shows FLIP-L on OpenImages for different token counts; even with only 100 patches, IoU remains near its peak, underscoring robust efficiency under constrained computational budgets.

Overall, these results highlight FLIP’s ability to accurately segment objects across scales, remain parameter-efficient, and adapt to variable computational budgets while matching or exceeding competing methods.

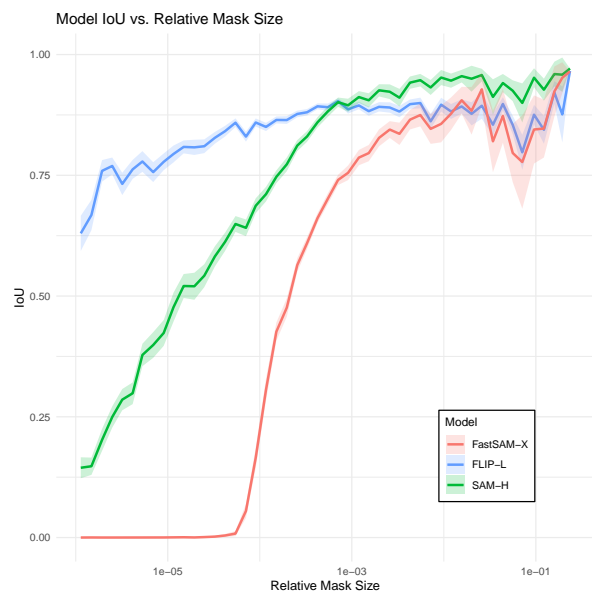


Figure 10. Intersection over Union (IoU) vs. relative mask size. FLIP maintains high segmentation accuracy even at extreme scales. Shaded regions show 95% confidence intervals.

## 5. Conclusion

We have introduced FLIP, a novel object-centric fovea-like input patching-based vision model that enhances scalable and data-efficient learning in complex visual scenes. FLIP implements a scale-invariant multi-resolution patch sampling mechanism, focusing high-resolution sampling around object centers using Gaussian distributions. As a result, FLIP effectively concentrates on critical regions while maintaining computational efficiency.

Our dynamic resolution mask prediction module and dedicated spatial attention mechanism, which separates perceptual and positional codes by applying positional embeddings exclusively to queries and keys, further improves



segmentation accuracy. This approach aligns with principles well-known in cognitive modeling and enhances spatial selectivity without compromising perceptual content.

Experimental results on our newly introduced ObjaScale dataset reveal that current state-of-the-art segmentation models lack a critical feature: effectively segmenting very small objects. FLIP fills this gap by maintaining strong accuracy for tiny objects through its fovea-like, scale-invariant patch sampling. Across synthetic datasets and standard benchmarks such as Hypersim, KITTI-360, and OpenImages, FLIP achieves competitive Intersection over Union (IoU) scores with higher efficiency. These findings highlight FLIP’s potential for significant impact in computer vision applications that require both robust and highly data-efficient, generalizable, fine-grained object segmentations.

## 6. Acknowledgement

This work received funding from the Deutsche Forschungsgemeinschaft (DFG, German Research Foundation) under Germany’s Excellence Strategy – EXC number 2064/1 – Project number 390727645 as well as from the Cyber Valley in Tübingen, CyVy-RF-2020-15. The authors thank the International Max Planck Research School for Intelligent Systems (IMPRS-IS) for supporting Manuel Traub, and the Alexander von Humboldt Foundation for supporting Martin Butz.

## References

- Chen, Y., Li, Y., Zhang, X., Sun, J., and Jia, J. Focal sparse convolutional networks for 3d object detection. In *Proceedings of the IEEE/CVF Conference on Computer Vision and Pattern Recognition*, pp. 5428–5437, 2022.
- Dai, J., Qi, H., Xiong, Y., Li, Y., Zhang, G., Hu, H., and Wei, Y. Deformable convolutional networks. In *Proceedings of the IEEE international conference on computer vision*, pp. 764–773, 2017.
- Deitke, M., Schwenk, D., Salvador, J., Weihs, L., Michel, O., VanderBilt, E., Schmidt, L., Ehsani, K., Kembhavi, A., and Farhadi, A. Objaverse: A universe of annotated 3d objects. In *Proceedings of the IEEE/CVF Conference on Computer Vision and Pattern Recognition (CVPR)*, pp. 13142–13153, June 2023.
- Dosovitskiy, A., Beyer, L., Kolesnikov, A., Weissenborn, D., Zhai, X., Unterthiner, T., Dehghani, M., Minderer, M., Heigold, G., Gelly, S., et al. An image is worth 16x16 words: Transformers for image recognition at scale. *arXiv preprint arXiv:2010.11929*, 2020.
- Elsayed, G., Mahendran, A., van Steenkiste, S., Greff, K., Mozer, M. C., and Kipf, T. Savi++: Towards end-to-end object-centric learning from real-world videos. In Koyejo, S., Mohamed, S., Agarwal, A., Belgrave, D., Cho, K., and Oh, A. (eds.), *Advances in Neural Information Processing Systems*, volume 35, pp. 28940–28954. Curran Associates, Inc., 2022.
- Jaegle, A., Borgeaud, S., Alayrac, J.-B., Doersch, C., Ionescu, C., Ding, D., Koppula, S., Zoran, D., Brock, A., Shelhamer, E., et al. Perceiver io: A general architecture for structured inputs & outputs. *arXiv preprint arXiv:2107.14795*, 2021.
- Kaplanyan, A. S., Sochenov, A., Leimkühler, T., Okunev, M., Goodall, T., and Rufo, G. Deepfovea: Neural reconstruction for foveated rendering and video compression using learned statistics of natural videos. *ACM Transactions on Graphics (TOG)*, 38(6):1–13, 2019.
- Kirillov, A., Mintun, E., Ravi, N., Mao, H., Rolland, C., Gustafson, L., Xiao, T., Whitehead, S., Berg, A. C., Lo, W.-Y., et al. Segment anything. In *Proceedings of the IEEE/CVF International Conference on Computer Vision*, pp. 4015–4026, 2023.
- Kuznetsova, A., Rom, H., Alldrin, N., Uijlings, J., Krasin, I., Pont-Tuset, J., Kamali, S., Popov, S., Mallocci, M., Kolesnikov, A., et al. The open images dataset v4: Unified image classification, object detection, and visual relationship detection at scale. *International journal of computer vision*, 128(7):1956–1981, 2020.
- Liao, Y., Xie, J., and Geiger, A. Kitti-360: A novel dataset and benchmarks for urban scene understanding in 2d and 3d. *IEEE Transactions on Pattern Analysis and Machine Intelligence*, 45(3):3292–3310, 2022.
- Liu, Z., Mao, H., Wu, C.-Y., Feichtenhofer, C., Darrell, T., and Xie, S. A convnet for the 2020s. In *Proceedings of the IEEE/CVF conference on computer vision and pattern recognition*, pp. 11976–11986, 2022.
- Locatello, F., Weissenborn, D., Unterthiner, T., Mahendran, A., Heigold, G., Uszkoreit, J., Dosovitskiy, A., and Kipf, T. Object-centric learning with slot attention. *Advances in Neural Information Processing Systems*, 33:11525–11538, 2020.
- Lukanov, H., König, P., and Pipa, G. Biologically inspired deep learning model for efficient foveal-peripheral vision. *Frontiers in Computational Neuroscience*, 15:746204, 2021.
- Roberts, M., Ramapuram, J., Ranjan, A., Kumar, A., Bautista, M. A., Paczan, N., Webb, R., and Susskind, J. M. Hypersim: A photorealistic synthetic dataset for holistic indoor scene understanding. In *Proceedings of the IEEE/CVF International Conference on Computer Vision (ICCV)*, pp. 10912–10922, October 2021.

- Singh, G., Wu, Y.-F., and Ahn, S. Simple unsupervised object-centric learning for complex and naturalistic videos. *Advances in Neural Information Processing Systems*, 35:18181–18196, 2022.
- Thavamani, C., Li, M., Cebren, N., and Ramanan, D. Fovea: Foveated image magnification for autonomous navigation. In *Proceedings of the IEEE/CVF international conference on computer vision*, pp. 15539–15548, 2021.
- Traub, M., Otte, S., Menge, T., Karlbauer, M., Thuemmel, J., and Butz, M. V. Learning what and where: Disentangling location and identity tracking without supervision. In *The Eleventh International Conference on Learning Representations*, 2023. URL [https://openreview.net/forum?id=NeDc-Ak-H\\_](https://openreview.net/forum?id=NeDc-Ak-H_).
- Traub, M., Becker, F., Otte, S., and Butz, M. V. Learning object permanence from videos via latent imaginations. In *International Conference on Artificial Neural Networks*, pp. 223–240. Springer, 2024a.
- Traub, M., Becker, F., Sauter, A., Otte, S., and Butz, M. V. Loci-segmented: improving scene segmentation learning. In *International Conference on Artificial Neural Networks*, pp. 45–61. Springer, 2024b.
- Xiong, R., Yang, Y., He, D., Zheng, K., Zheng, S., Xing, C., Zhang, H., Lan, Y., Wang, L., and Liu, T. On layer normalization in the transformer architecture. In *International Conference on Machine Learning*, pp. 10524–10533. PMLR, 2020.
- Xiong, Y., Li, Z., Chen, Y., Wang, F., Zhu, X., Luo, J., Wang, W., Lu, T., Li, H., Qiao, Y., et al. Efficient deformable convnets: Rethinking dynamic and sparse operator for vision applications. In *Proceedings of the IEEE/CVF Conference on Computer Vision and Pattern Recognition*, pp. 5652–5661, 2024.
- Yu, R., Wang, Z., Wang, Y., Li, K., Liu, C., Duan, H., Ji, X., and Chen, J. Lape: Layer-adaptive position embedding for vision transformers with independent layer normalization. In *Proceedings of the IEEE/CVF International Conference on Computer Vision*, pp. 5886–5896, 2023.
- Zaal, Greg. Hdri haven, 2016. URL <https://hdri-haven.com/>. Accessed: 2024-11-20.
- Zadaianchuk, A., Seitzer, M., and Martius, G. Object-centric learning for real-world videos by predicting temporal feature similarities. *Advances in Neural Information Processing Systems*, 36, 2024.
- Zhao, X., Ding, W., An, Y., Du, Y., Yu, T., Li, M., Tang, M., and Wang, J. Fast segment anything, 2023.
- Zhu, X., Hu, H., Lin, S., and Dai, J. Deformable convnets v2: More deformable, better results. In *Proceedings of the IEEE/CVF conference on computer vision and pattern recognition*, pp. 9308–9316, 2019.